(Received 2 April 2025, Accepted 26 May 2025, Scheduled 3 June 2025)

Bernoulli Filter for Low-Grazing Angle Track-before-Detect with Monopulse Radar

Fei Cai*

College of Information Science and Engineering, Hunan Normal University, Changsha 410081, Hunan, China

ABSTRACT: Target tracking in a low-grazing angle scenario is a challenging problem in radar because of multipath phenomenon. When the signal-to-noise ratio (SNR) is low, this problem becomes more difficult. This paper applies a Bernoulli filter for low-grazing angle track-before-detect with monopulse radar. A measurement model is established using Swerling II radar target model. The filter is implemented approximately as a particle filter. Simulation results show that the proposed filter is effective at detection and tracking in a multipath scenario and under low SNR.

1. INTRODUCTION

When radar tracks a low-elevation target, since the grazing angle of the target is low, in addition to the direct echo, reflection signals from the ground or sea surface also enter the radar beam. An illustration of target tracking in a low-grazing angle scenario is shown in Fig. 1. In this scenario, the radar observes two targets: the true target above the surface and its mirror image below the surface. Because the range and Doppler differences between the target and its image are generally small compared to radar resolutions, target echoes from direct and reflected paths often occupy the same beam and resolution bin (range and/or Doppler). Consequently, monopulse processing commonly used in tracking radars to estimate the direction of arrival (DOA) may fail. Target tracking in low-grazing angle (LGA) scenarios remains a well-recognized challenge in the radar community [1–3].

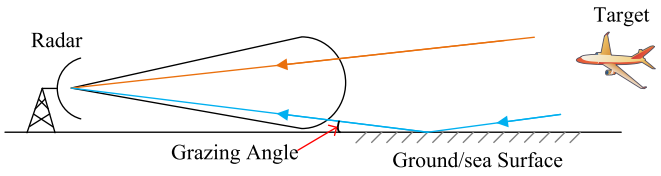

FIGURE 1. Illustration of the low-grazing angle scenario.

For monopulse radar, DOA is typically estimated using the real part of the monopulse ratio. If two or more targets fall into the same resolution bin and beam due to limited radar resolution, the typical monopulse processing may fail because the monopulse ratio is affected by all the unresolved targets in that bin. The DOA estimation wanders as the relative phases and amplitudes of the unresolved targets change, and it may not be true for any of them. Unresolved targets detection and estimation have been active areas of research over the past several decades [4–12]. Joint detection and tracking of unresolved targets using a particle filter was studied in [13–15].

In LGA scenario, the target and its image can be treated as two unresolved targets. As a result, the DOA estimation of the typical monopulse processing does not correspond to the DOA of the target or its image. The estimation methods for unresolved targets may be used to estimate the DOA of the target in an LGA scenario. However, unlike the general unresolved targets, there exists a constraint relationship between the target and its image. This constraint relationship includes the geometric relationship and the signal magnitude relationship. By fully utilizing these constraints, the estimation performance may be improved. To achieve this, it is critical to accurately model the multipath propagation.

There are many researches on low-grazing angle tracking, including array signal processing methods [16, 17] and enhanced monopulse methods [18, 19]. In recent years, with the development of tracking theory, LGA tracking based on multipath propagation modeling and particle filtering has attracted academic attention. Ref. [1] investigated low-angle tracking using Orthogonal Frequency Division Multiplexing (OFDM) Multiple-Input Multiple-Output (MIMO) radar, implemented with a particle filter and verified the importance of accurate multipath propagation modeling. Ref. [20] studied tracking issues in the context of sea-surface multipath based on particle filtering, considering both specular reflection and diffuse reflection. The results indicated that an increase in the number of reflection paths helps improve estimation performance. These studies demonstrate that modeling multipath propagation within the filter can transform the issue of multipath interference into an opportunity for multipath utilization. By comprehensively leveraging multipath echoes and direct waves, tracking problems in multipath environments can be addressed. However, the aforementioned studies are all based on the traditional detect-before-track architecture. When the signal-to-noise ratio is low, missed detections and false alarms of targets may render these methods ineffective. Multipath reflections are also used in the localization of non-line-of-sight (NLOS) targets [21, 22].

* Corresponding author: Fei Cai (caifei@hunnu.edu.cn).

Track-before-detect (TBD) is an efficient dim target tracking method. It outperforms conventional methods in low SNR scenarios through joint detection and tracking using unthresholded data or thresholded data with extremely low thresholds [23–25]. The commonly used TBD techniques include Hough transform [24], dynamic programming [23], Particle filter based TBD (PF-TBD) [26–28], and histogram probabilistic multi-hypothesis tracking (H-PMHT) algorithm [29]. Bernoulli filter is an optimal joint detection and tracking filter for a single target [30–32]. Different measurement models can be used in Bernoulli filter, resulting in different update equations. Detector output model and intensity measurement model are two commonly used measurement models in Bernoulli filter, with the latter resulting in Bernoulli TBD filter. Bernoulli TBD filter has been employed in several radar applications, such as MIMO radar [33], scanning maritime radar [34, 35], monopulse radar [36], and staring array radar [37].

In this article, we use a Bernoulli TBD filter to address the detection and tracking problem in a low-grazing angle scenario using a monopulse radar. First, we develop state-space model and multipath model to capture the constraint relationship between the target and its image. Second, we develop the measurement model of the monopulse radar using Swerling II target model and point spread function. Third, we use a Bernoulli filter to estimate the target's presence and state, and implement the Bernoulli filter using a particle filter. Finally, simulations are used to evaluate the performance of the proposed method. The results show that the target's presence and DOA can be efficiently estimated in the presence of multipath echo in a low SNR scenario. The main contributions of this article are summarized as follows.

1) State-space model and multipath model are developed for LGA scenario.
2) The measurement model using Swerling II target model and point spread function is developed for a monopulse radar, which has considered all three cases.
3) A Bernoulli TBD filter and its particle filter implementation are developed for LGA scenario. Simulation results demonstrate the effectiveness of the proposed method.

The rest of this article is organized as follows. In Section 2, target models and multipath model are established. In Section 3, measurement model is developed. In Section 4, the Bernoulli filter and its particle filter implementation are presented. In Section 5, the simulation results are presented. Finally, Section 6 concludes this article.

2. MODELS

2.1. Target State Model

In the low angle tracking scenario, the main challenge lies in the estimation of the vertical angle. Hence, we consider a 2-D case in which radar estimates the vertical DOA only. We assume that there is at most one target in the scene, and the target can be absent or present. The state vector of the target is denoted as $\mathbf{x} = [x, \dot{x}, y, \dot{y}]^T$, where (x, y) is the Cartesian coordinates of the target position, and $(\dot{x}, \dot{y})$ is the target velocity vector. Using the Finite Set Statistics (FISST), the target state is modeled as a Bernoulli random finite set (RFS) X. If the target is present, X has one element and can be expressed as $X = \{\mathbf{x}\}$; otherwise, it is empty, that is, $X = \emptyset$. Thus, at time step k, the probability density of the target state X is given by

$$f_{k|k}(X) = \begin{cases} 1 - p_{k|k} & \text{if } X = \emptyset \\ p_{k|k} f_{k|k}(\mathbf{x}) & \text{if } X = \{\mathbf{x}\} \end{cases} \tag{1}$$

where $f_{k|k}(\mathbf{x})$ is the probability density of the target state vector, and $p_{k|k}$ is the probability of target existence.

2.2. Target Dynamic Model

Without loss of generality, a nearly constant velocity model is used to model the target motion, that is

$$\mathbf{x}_k = \mathbf{F}\mathbf{x}_{k-1} + \mathbf{w}_k \tag{2}$$

where $\mathbf{F}$ is the transition matrix, and $\mathbf{w}_k$ is the white Gaussian process noise with a distribution given by $\mathbf{w}_k \sim \mathcal{N}(0, \mathbf{Q})$, with $\mathbf{F}$ and $\mathbf{Q}$ given by [38]

$$\mathbf{F} = \begin{pmatrix} 1 & T & 0 & 0 \\ 0 & 1 & 0 & 0 \\ 0 & 0 & 1 & T \\ 0 & 0 & 0 & 1 \end{pmatrix} \tag{3}$$

$$\mathbf{Q} = \sigma_w^2 \begin{pmatrix} \frac{1}{4}T^4 & \frac{1}{2}T^3 & 0 & 0 \\ \frac{1}{2}T^3 & T^2 & 0 & 0 \\ 0 & 0 & \frac{1}{4}T^4 & \frac{1}{2}T^3 \\ 0 & 0 & \frac{1}{2}T^3 & T^2 \end{pmatrix} \tag{4}$$

where T is the interval between the time steps, and σ_w^2 is the variance of the process noise.

The existence of the target is modeled by a first-order two-state Markov chain. If the target does not exist at time step $k-1$, it may enter the scene at time step k with probability p_B and birth density $b_{k|k-1}(\mathbf{x})$, or it may remain absent from the scene with probability $1 - p_B$. Thus, the target state X at time step k is a Bernoulli RFS, and the Markov density is given by

$$f_{k|k-1}(X|\emptyset) = \begin{cases} 1 - p_B & \text{if } X = \emptyset \\ p_B b_{k|k-1}(\mathbf{x}) & \text{if } X = \{\mathbf{x}\} \end{cases} \tag{5}$$

On the other hand, if a target with state $\mathbf{x}'$ is present at time step $k-1$, it is assumed that the target can survive to the next time step k with probability p_S and transition to state $\mathbf{x}$ with density $f_{k|k-1}(\mathbf{x}|\mathbf{x}')$, or disappear from the scene with probability $1 - p_S$. The dynamics of the target state vector between two consecutive time steps is given by $f_{k|k-1}(\mathbf{x}|\mathbf{x}') = \mathcal{N}(\mathbf{x}; \mathbf{F}\mathbf{x}', \mathbf{Q})$ in this article, according to (2). In this scenario, the target state X at time step k is also a Bernoulli RFS, and the Markov density is specified by

$$f_{k|k-1}(X|\{\mathbf{x}'\}) = \begin{cases} 1 - p_S & \text{if } X = \emptyset \\ p_S f_{k|k-1}(\mathbf{x}|\mathbf{x}') & \text{if } X = \{\mathbf{x}\} \end{cases} \tag{6}$$

2.3. Multipath Model

For simplicity, consider the flat-Earth multipath model as shown in Fig. 2, where h_r and h_t are the heights of the radar antenna phase centre and the target, respectively; r_d and $r_r = r_1 + r_2$ are the lengths of the direct and reflected paths, respectively; θ_d and θ_r are the incident angles of the target and the image, respectively. Flat-Earth model is appropriate for the case where the target range is not large, if it is not the case, a more general multipath model considering the curvature of the earth should be used [1].

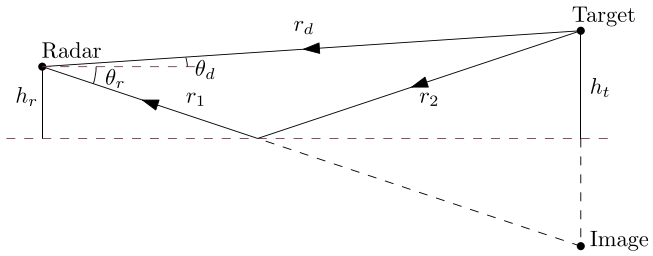

FIGURE 2. Flat-Earth multipath model.

Assume that the radar is stationary and located at Cartesian coordinates $(0, h_r)$. Since the Cartesian coordinates of the target are (x, y), the coordinates of the image are $(x, -y)$. Thus, r_d, r_r, θ_d, and θ_r can be calculated by

$$r_d = \sqrt{x^2 + (y - h_r)^2} \tag{7}$$

$$\theta_d = \arctan\left((y - h_r)/x\right) \tag{8}$$

$$r_r = \sqrt{x^2 + (y + h_r)^2} \tag{9}$$

$$\theta_r = \arctan\left((-y - h_r)/x\right) \tag{10}$$

The multipath reflection signals include specular reflection signal and diffuse reflection signals. The specular reflection is dominant for smooth surfaces, while the diffuse reflection is dominant for rough surfaces. Only the specular multipath is considered in this article. The specular reflection coefficient is denoted as ρ, and it generally consists of three factors: Fresnel reflection coefficient ρ_0, divergence factor D, and surface roughness factor ρ_s. The Fresnel reflection coefficient is a function of the grazing angle, radar polarization, and electromagnetic properties of the reflecting surface. The function is given by

$$\rho_0 = \begin{cases} \dfrac{\epsilon \sin\theta_r - \sqrt{\epsilon - (\cos\theta_r)^2}}{\epsilon \sin\theta_r + \sqrt{\epsilon - (\cos\theta_r)^2}} & \text{vertical polarization} \\ \dfrac{\sin\theta_r - \sqrt{\epsilon - (\cos\theta_r)^2}}{\sin\theta_r + \sqrt{\epsilon - (\cos\theta_r)^2}} & \text{horizontal polarization} \end{cases} \tag{11}$$

where $\epsilon = \epsilon' - j60\lambda\sigma$ is the relative permittivity at the reflecting surface, ϵ' the relative dielectric constant of the reflecting surface, λ the radar wavelength, and σ the conductivity of the reflecting surface. The divergence factor D is given by

$$D \approx \left(1 + \frac{2h_r(r_d \sin\theta_d + h_r)}{r_e r_d \cos\theta_d \sin^3\theta_r}\right)^{-1/2} \tag{12}$$

where r_e is the earth radius. The surface roughness factor ρ_s is given by

$$\rho_s = \exp\left(-8\pi^2 \left(\frac{h_{\text{rms}} \sin\theta_r}{\lambda}\right)^2\right) \tag{13}$$

where h_{rms} is the root-mean-square (RMS) surface height variation. The specular reflection coefficient ρ is calculated by

$$\rho = \rho_0 D \rho_s \tag{14}$$

3. MONOPULSE RETURNS

Swerling II radar target model is adopted in this article, in which the target amplitude is pulse-to-pulse independent and follows a Rayleigh distribution. This can be achieved through frequency diversity among the pulses [39]. Under this assumption, the target radar cross section (RCS) σ has an exponential distribution

$$p(\sigma) = \frac{1}{\bar{\sigma}} \exp\left(-\frac{\sigma}{\bar{\sigma}}\right) \tag{15}$$

where $\bar{\sigma}$ is the average RCS of the target. In this study $\bar{\sigma}$ is assumed to be constant and known. The square of the signal amplitude α is proportional to σ (i.e., $\alpha^2 \propto \sigma$), and thus α has a Rayleigh distribution

$$p(\alpha) = \frac{\alpha}{\alpha_0^2} \exp\left(-\frac{\alpha^2}{2\alpha_0^2}\right) \tag{16}$$

where $E[\alpha^2] = 2\alpha_0^2 \propto \bar{\sigma}$.

As in [10], we assume that the radar waveform has a rectangular envelope of width τ, then its matched filter output has a triangular envelope of width 2τ. Let the matched filter sampling rate be $1/\tau$, then there are two contiguous sampling points affected by the target (or image). Denote the space between two contiguous sampling points as a slot, then the size of a slot is $\Delta R = c\tau/2$. Assume that there are L sampling points for each pulse. Denote the first and second sampling points affected by the target (or image) as l_1 and l_2, respectively, then the contributions of a target (or image) at range r to the two sampling points are, respectively, $h_{l_1}(r) = 1 - \text{mod}(r, \Delta R)/\Delta R$ and $h_{l_2}(r) = \text{mod}(r, \Delta R)/\Delta R$.

Since the length of the direct path is smaller than that of the reflected path, we have $r_d < r_r$. There are three possible cases of the target and image locations in the slots. Fig. 3 shows the three cases and the resulting matched filter outputs.

3.1. Case I --- Target and Image Located in One Slot

In Case I, the target and its image are located within one slot as shown in Fig. 3(a). There are two sampling points affected by them, and both are the result of their superposition. The matched filter outputs consist of four samples at each sampling point, namely: the in-phase and quadrature parts of the sum and difference signals.

The matched filter outputs at the two sampling points l_1 and l_2 can be written as

$$\begin{aligned}
s_I(l_1) &= \alpha_{1d}\cos\phi_d + \alpha_{1r}\cos\phi_r + n_{sI}(l_1)\\
s_I(l_2) &= \alpha_{2d}\cos\phi_d + \alpha_{2r}\cos\phi_r + n_{sI}(l_2)\\
s_Q(l_1) &= \alpha_{1d}\sin\phi_d + \alpha_{1r}\sin\phi_r + n_{sQ}(l_1)\\
s_Q(l_2) &= \alpha_{2d}\sin\phi_d + \alpha_{2r}\sin\phi_r + n_{sQ}(l_2)\\
d_I(l_1) &= \gamma_d\alpha_{1d}\cos\phi_d + \gamma_r\alpha_{1r}\cos\phi_r + n_{dI}(l_1)\\
d_I(l_2) &= \gamma_d\alpha_{2d}\cos\phi_d + \gamma_r\alpha_{2r}\cos\phi_r + n_{dI}(l_2)\\
d_Q(l_1) &= \gamma_d\alpha_{1d}\sin\phi_d + \gamma_r\alpha_{1r}\sin\phi_r + n_{dQ}(l_1)\\
d_Q(l_2) &= \gamma_d\alpha_{2d}\sin\phi_d + \gamma_r\alpha_{2r}\sin\phi_r + n_{dQ}(l_2)
\end{aligned} \tag{17}$$

where α_{id} $(i = 1, 2)$ and α_{ir} $(i = 1, 2)$ denote the signal amplitudes of the direct and reflected echoes, respectively, at the ith sampling point that it affected. γ_d and γ_r denote the "electronic angle" of the direct and reflected paths, respectively. $[\alpha_{id}, \gamma_d]^T$ and $[\alpha_{ir}, \gamma_r]^T$ are related to the target state $\mathbf{x}$ using (7)–(10) and the following equations

$$\begin{aligned}
\alpha_{id} &= \frac{\kappa\sqrt{\sigma}h_{l_i}(r_d)G_\Sigma^2(\theta_d-\theta_p)}{r_d^2},\ \gamma_d = \frac{G_\Delta(\theta_d-\theta_p)}{G_\Sigma(\theta_d-\theta_p)}\\
\alpha_{ir} &= \frac{\kappa\rho\sqrt{\sigma}h_{l_i}(r_r)G_\Sigma^2(\theta_r-\theta_p)}{r_r^2},\ \gamma_r = \frac{G_\Delta(\theta_r-\theta_p)}{G_\Sigma(\theta_r-\theta_p)}
\end{aligned} \tag{18}$$

where κ is a constant of the radar determined by the radar equation [40]; θ_p is the radar boresight angle; $G_\Sigma(\theta)$ and $G_\Delta(\theta)$ are the sum and difference beam patterns at angle θ, respectively. The phases ϕ_d and ϕ_r are the received phased angles of the target and its image, respectively. They are assumed to be uniformly distributed on $[0, 2\pi)$ and independent of each other. The matched filter outputs at the other sampling points contain noise only. The noises $n_{sI}(l)$, $n_{sQ}(l)$, $n_{dI}(l)$, and $n_{dQ}(l)$ $(l = 1, \ldots, L)$ are independent, zero-mean, and Gaussian, with variances

$$\begin{aligned}
E[n_{sI}(l)^2] = E[n_{sQ}(l)^2] = \sigma_s^2\\
E[n_{dI}(l)^2] = E[n_{dQ}(l)^2] = \sigma_d^2
\end{aligned} \tag{19}$$

The signal vector in this case has form

$$\begin{aligned}
\mathbf{g} \;=\; &[s_I(l_1), s_I(l_2), d_I(l_1), d_I(l_2), s_Q(l_1),\\
&s_Q(l_2), d_Q(l_1), d_Q(l_2)]^T
\end{aligned} \tag{20}$$

Then, we have $p(\mathbf{g}|\mathbf{x}) = \mathcal{N}(\mathbf{g}; 0, \mathbf{P})$, where

$$\mathbf{P} = \begin{bmatrix} \mathbf{P}_1 & 0 \\ 0 & \mathbf{P}_1 \end{bmatrix} \tag{21}$$

and

$$\mathbf{P}_1 = \begin{bmatrix} \alpha_{01d}^2 & \alpha_{01d}\alpha_{02d} & \alpha_{01d}^2\gamma_d & \alpha_{01d}\alpha_{02d}\gamma \\ & \alpha_{02d}^2 & \alpha_{01d}\alpha_{02d}\gamma_d & \alpha_{02d}^2\gamma_d \\ & & \alpha_{01d}^2\gamma_d^2 & \alpha_{01d}\alpha_{02d}\gamma_d^2 \\ & & & \alpha_{02d}^2\gamma_d^2 \end{bmatrix}$$

$$+\begin{bmatrix} \alpha_{01r}^2 & \alpha_{01r}\alpha_{02r} & \alpha_{01r}^2\gamma_r & \alpha_{01r}\alpha_{02r}\gamma \\ & \alpha_{02r}^2 & \alpha_{01r}\alpha_{02r}\gamma_r & \alpha_{02r}^2\gamma_r \\ & & \alpha_{01r}^2\gamma_r^2 & \alpha_{01r}\alpha_{02r}\gamma_r^2 \\ & & & \alpha_{02r}^2\gamma_r^2 \end{bmatrix}$$

$$+\text{diag}(\sigma_s^2, \sigma_s^2, \sigma_d^2, \sigma_d^2) \tag{22}$$

where α_{0id} and α_{0ir} are the Rayleigh parameters corresponding to α_{id} and α_{ir}, respectively. Because matrix $\mathbf{P}_1$ is symmetric, we present only the upper triangular elements here.

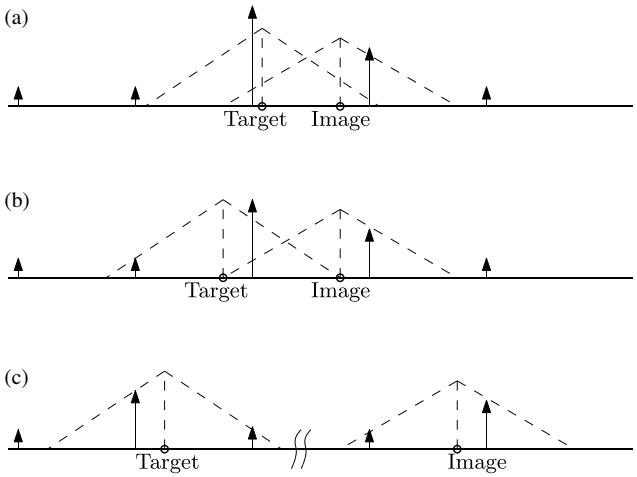

FIGURE 3. The three cases of the target and image locations. (a) Case I. (b) Case II. (c) Case III.

3.2. Case II --- Target and Image Located in Two Neighboring Slots

As shown in Fig. 3(b), in this case, the target and image are located in two neighboring slots. There are three sampling points l_1, l_2, and l_3 affected by them, and only l_2 is the superposition of their signals. The matched filter outputs at the three sampling points can be written as follows:

$$\begin{aligned}
s_I(l_1) &= \alpha_{1d}\cos\phi_d + n_{sI}(l_1)\\
s_I(l_2) &= \alpha_{2d}\cos\phi_d + \alpha_{1r}\cos\phi_r + n_{sI}(l_2)\\
s_I(l_3) &= \alpha_{2r}\cos\phi_r + n_{sI}(l_3)\\
s_Q(l_1) &= \alpha_{1d}\sin\phi_d + n_{sQ}(l_1)\\
s_Q(l_2) &= \alpha_{2d}\sin\phi_d + \alpha_{1r}\sin\phi_r + n_{sQ}(l_2)\\
s_Q(l_3) &= \alpha_{2r}\sin\phi_r + n_{sQ}(l_3)\\
d_I(l_1) &= \gamma_d\alpha_{1d}\cos\phi_d + n_{dI}(l_1)\\
d_I(l_2) &= \gamma_d\alpha_{2d}\cos\phi_d + \gamma_r\alpha_{1r}\cos\phi_r + n_{dI}(l_2)\\
d_I(l_3) &= \gamma_r\alpha_{2r}\cos\phi_r + n_{dI}(l_3)\\
d_Q(l_1) &= \gamma_a\alpha_{1d}\sin\phi_d + n_{dQ}(l_1)\\
d_Q(l_2) &= \gamma_a\alpha_{2d}\sin\phi_d + \gamma_r\alpha_{1r}\sin\phi_r + n_{dQ}(l_2)\\
d_Q(l_3) &= \gamma_r\alpha_{2r}\sin\phi_r + n_{dQ}(l_3)
\end{aligned} \tag{23}$$

The signal vector has form

$$\begin{aligned}
\mathbf{g} \;=\; &[s_I(l_1), s_I(l_2), s_I(l_3), d_I(l_1), d_I(l_2), d_I(l_3), s_Q(l_1),\\
&s_Q(l_2), s_Q(l_3), d_Q(l_1), d_Q(l_2), d_Q(l_3)]^T
\end{aligned} \tag{24}$$

$$\mathbf{P}_1 = \begin{bmatrix} \alpha_{01d}^2 & \alpha_{01d}\alpha_{02d} & 0 & \alpha_{01d}^2\gamma_d & \alpha_{01d}\alpha_{02d}\gamma_d & 0 \\ & \alpha_{02d}^2+\alpha_{01r}^2 & \alpha_{01r}\alpha_{02r} & \alpha_{01d}\alpha_{02d}\gamma_d & \alpha_{02d}^2\gamma_d+\alpha_{01r}^2\gamma_r & \alpha_{01r}\alpha_{02r}\gamma_r \\ & & \alpha_{02r}^2 & 0 & \alpha_{01r}\alpha_{02r}\gamma_r & \alpha_{02r}^2\gamma_r \\ & & & \alpha_{01d}^2\gamma_d^2 & \alpha_{01d}\alpha_{02d}\gamma_d^2 & 0 \\ & & & & \alpha_{02d}^2\gamma_d^2+\alpha_{01r}^2\gamma_r^2 & \alpha_{01r}\alpha_{02r}\gamma_r^2 \\ & & & & & \alpha_{02r}^2\gamma_r^2 \end{bmatrix} + \text{diag}(\sigma_s^2,\sigma_s^2,\sigma_s^2,\sigma_d^2,\sigma_d^2,\sigma_d^2) \quad (25)$$

3.3. Case III --- Target and Image Located in Two Disconnected Slots

As shown in Fig. 3(c), in this case, the range difference between target and image is more than $2\Delta R$, and four sampling points are affected by them. As the matched filter outputs of the target and its image are not overlapped, they can be considered separately. The signal vector is $\mathbf{g} = [\mathbf{g}_d^T, \mathbf{g}_r^T]^T$, which consists of direct signal $\mathbf{g}_d$ and reflected signal $\mathbf{g}_r$, with

$$\begin{aligned} \mathbf{g}_d &= [s_I(l_1), s_I(l_2), d_I(l_1), d_I(l_2), s_Q(l_1), \\ &\quad s_Q(l_2), d_Q(l_1), d_Q(l_2)]^T \\ \mathbf{g}_r &= [s_I(l_3), s_I(l_4), d_I(l_3), d_I(l_4), s_Q(l_3), \\ &\quad s_Q(l_4), d_Q(l_3), d_Q(l_4)]^T \end{aligned} \quad (26)$$

Then, $p(\mathbf{g}|\mathbf{x}) = \mathcal{N}(\mathbf{g}_d; 0, \mathbf{P})\mathcal{N}(\mathbf{g}_r; 0, \mathbf{P})$, where $\mathbf{P}$ has the same structure as shown in (21), and the $\mathbf{P}_1$ in $\mathbf{P}$ (taking $\mathbf{g}_d$ as an example) has the following form:

$$\mathbf{P}_1 = \begin{bmatrix} \alpha_{01d}^2 & \alpha_{01d}\alpha_{02d} & \alpha_{01d}^2\gamma_d & \alpha_{01d}\alpha_{02d}\gamma_d \\ & \alpha_{02d}^2 & \alpha_{01d}\alpha_{02d}\gamma_d & \alpha_{02d}^2\gamma_d \\ & & \alpha_{01d}^2\gamma_d^2 & \alpha_{01d}\alpha_{02d}\gamma_d^2 \\ & & & \alpha_{02d}^2\gamma_d^2 \end{bmatrix} + \text{diag}\left(\sigma_s^2, \sigma_s^2, \sigma_d^2, \sigma_d^2\right) \quad (27)$$

3.4. The Likelihood Ratio

We assume that the radar sends M pulses in each dwell (we set the dwells as the time steps in the TBD filter), and the returns from different pulses are independent and identically distributed (IID). Denote $\mathbf{G} = \{\mathbf{g}_m\}_{m=1}^M$, where $\mathbf{g}_m$ is the signal vector of the mth pulse. Then, we have

$$p(\mathbf{G}|\mathbf{x}) = \prod_{m=1}^{M} p(\mathbf{g}_m|\mathbf{x}) \quad (28)$$

The sampling points not affected by the target and image contain only noise. If there is no target in the scene, all the sampling points contain only noise. We have an observation vector from the mth pulse as $\mathbf{z}_m = \{\mathbf{z}_{ml}\}_{l=1}^L$, where $\mathbf{z}_{ml} = [s_I(l), d_I(l), s_Q(l), d_Q(l)]^T$. Then, the likelihood for sampling points containing only noise is

$$p(\mathbf{z}_{ml}|\emptyset) = \mathcal{N}(\mathbf{z}_{ml}; 0, \mathbf{P}') \quad (29)$$

where $\mathbf{P}' = \text{diag}(\sigma_s^2, \sigma_d^2, \sigma_s^2, \sigma_d^2)$.

All the observation vectors in the M pulses constitute the measurement for the TBD filter: $\mathbf{z} = \{\mathbf{z}_m\}_{m=1}^M$. The sampling points that contain only noise have the same probability density function (PDF) under both hypotheses: either the target is present ($X = \{\mathbf{x}\}$) or not ($X = \emptyset$). Then, the likelihood ratio $\ell(\mathbf{z}|\mathbf{x}) \triangleq \frac{p(\mathbf{z}|\{\mathbf{x}\})}{p(\mathbf{z}|\emptyset)}$ is determined solely by the sampling points affected by $\mathbf{x}$. Specifically,

$$\ell(\mathbf{z}|\mathbf{x}) = \frac{p(\mathbf{G}|\{\mathbf{x}\})}{p(\mathbf{G}|\emptyset)} = \frac{\prod_{m=1}^M \mathcal{N}(\mathbf{g}_m; 0, \mathbf{P})}{\prod_{m=1}^M \prod_{l\in S(\mathbf{x})} \mathcal{N}(\mathbf{z}_{ml}; 0, \mathbf{P}')} \quad (30)$$

where $S(\mathbf{x})$ is the set of sampling points affected by the target and image.

4. THE BERNOULLI TRACK-BEFORE-DETECT FILTER

4.1. The Analytical Expressions

The goal of the track-before-detect filter is to detect the existence of a target and estimate its state $\mathbf{x}$ if it is present. To achieve this, the two posteriors are first estimated recursively using the Bayesian filtering: 1) the probability of target existence $p_{k|k}$; 2) the posterior probability density of the target state, $f_{k|k}(\mathbf{x})$. The detection of target existence is then done using $p_{k|k}$ as the test statistic. If the target is detected, the target state is estimated using $f_{k|k}(\mathbf{x})$.

If the probability of target existence $p_{k-1|k-1}$ and posterior probability density $f_{k-1|k-1}(\mathbf{x})$ at time step $k-1$ are given, the recursion of the Bernoulli TBD filter is as follows [31].

Predictor:

$$p_{k|k-1} = p_b(1-p_{k-1|k-1}) + p_s p_{k-1|k-1} \quad (31)$$

$$f_{k|k-1}(\mathbf{x}) = \frac{p_b b_{k|k-1}(\mathbf{x})(1-p_{k-1|k-1})}{p_{k|k-1}} + \frac{p_s p_{k-1|k-1} \int f_{k|k-1}(\mathbf{x}|\mathbf{x}') f_{k-1|k-1}(\mathbf{x}')d\mathbf{x}'}{p_{k|k-1}} \quad (32)$$

Corrector:

$$p_{k|k} = \frac{p_{k|k-1}\int \ell(\mathbf{z}|\mathbf{x}) f_{k|k-1}(\mathbf{x})d\mathbf{x}}{1-p_{k|k-1}+p_{k|k-1}\int \ell(\mathbf{z}_k|\mathbf{x}) f_{k|k-1}(\mathbf{x})d\mathbf{x}} \quad (33)$$

$$f_{k|k}(\mathbf{x}) = \frac{\ell(\mathbf{z}|\mathbf{x}) f_{k|k-1}(\mathbf{x})}{\int \ell(\mathbf{z}|\mathbf{x}) f_{k|k-1}(\mathbf{x})d\mathbf{x}} \quad (34)$$

4.2. The Particle Filter Implementation

Sequential Monte Carlo method is used to implement the Bernoulli TBD filter. The probability density $f_{k|k}(\mathbf{x})$ is approximated by a particle system $\{w_k^{(n)}, \mathbf{x}_k^{(n)}\}_{n=1}^N$. That is,

$$f_{k|k}(\mathbf{x}) \approx \sum_{n=1}^{N} w_k^{(n)} \delta_{\mathbf{x}_k^{(n)}}(\mathbf{x}) \tag{35}$$

where $\mathbf{x}_k^{(n)}$ and $w_k^{(n)}$ are the state and weight of the nth particle, respectively, and $\delta_{\mathbf{b}}(\mathbf{x})$ is the Dirac delta function concentrated at point $\mathbf{b}$. The weights are normalized such that $\sum_{n=1}^N w_k^{(n)} = 1$.

If $p_{k-1|k-1}$ and particles $\{w_{k-1}^{(n)}, \mathbf{x}_{k-1}^{(n)}\}_{n=1}^N$ that approximate $f_{k-1|k-1}(\mathbf{x})$ at time step $k-1$ are given, the recursion of the particle filter implementation of the Bernoulli TBD filter is as follows [36].

Predictor:

The probability of existence $p_{k|k-1}$ is predicted firstly using (31). Then, according to (32), the prediction of $f_{k|k-1}(\mathbf{x})$ is composed of two parts, the new birth and the persisting. We use N and B particles to approximate the persisting and the new birth components, respectively. The particles are drawn from two proposal distributions:

$$\mathbf{x}_{k|k-1}^{(n)} \sim \begin{cases} f_{k|k-1}(\mathbf{x}|\mathbf{x}_{k-1}^{(n)}) & n = 1, \ldots, N \\ b_{k|k-1}(\mathbf{x}) & n = N+1, \ldots, N+B \end{cases} \tag{36}$$

with weights

$$w_{k|k-1}^{(n)} = \begin{cases} \frac{p_s p_{k-1|k-1}}{N p_{k|k-1}} & n = 1, \ldots, N \\ \frac{p_b(1-p_{k-1|k-1})}{B p_{k|k-1}} & n = N+1, \ldots, N+B \end{cases} \tag{37}$$

Then, the particle approximation of $f_{k|k-1}(\mathbf{x})$ can be expressed as

$$f_{k|k-1}(\mathbf{x}) \approx \sum_{n=1}^{N+B} w_{k|k-1}^{(n)} \delta_{\mathbf{x}_{k|k-1}^{(n)}}(\mathbf{x}) \tag{38}$$

To reduce computational complexity, compute $w'^{(n)}_{k|k-1}$ instead of $w_{k|k-1}^{(n)}$ as follows:

$$w'^{(n)}_{k|k-1} = \begin{cases} p_s p_{k-1|k-1}/N & n = 1, \ldots, N \\ p_b(1-p_{k-1|k-1})/B & n = N+1, \ldots, N+B \end{cases} \tag{39}$$

Corrector:

The integral in (33) and (34) is approximated by

$$\int \ell(\mathbf{z}|\mathbf{x}) f_{k|k-1}(\mathbf{x}) d\mathbf{x} \approx \sum_{n=1}^{N+B} w_{k|k-1}^{(n)} \ell(\mathbf{z}|\mathbf{x}_{k|k-1}^{(n)}) \tag{40}$$

Then, (33) is approximated by

$$p_{k|k} \approx \frac{p_{k|k-1} \sum_{n=1}^{N+B} w_{k|k-1}^{(n)} \ell(\mathbf{z}|\mathbf{x}_{k|k-1}^{(n)})}{1 - p_{k|k-1} + p_{k|k-1} \sum_{n=1}^{N+B} w_{k|k-1}^{(n)} \ell(\mathbf{z}|\mathbf{x}_{k|k-1}^{(n)})}$$

$$= \frac{\sum_{n=1}^{N+B} w'^{(n)}_{k|k-1} \ell(\mathbf{z}_k|\mathbf{x}_{k|k-1}^{(n)})}{1 - p_{k|k-1} + \sum_{n=1}^{N+B} w'^{(n)}_{k|k-1} \ell(\mathbf{z}|\mathbf{x}_{k|k-1}^{(n)})} \tag{41}$$

and (34) is approximated by

$$f_{k|k}(\mathbf{x}) \approx \frac{\sum_{n=1}^{N+B} \ell(\mathbf{z}|\mathbf{x}_{k|k-1}^{(n)}) w_{k|k-1}^{(n)} \delta_{\mathbf{x}_{k|k-1}^{(n)}}(\mathbf{x})}{\sum_{n=1}^{N+B} \ell(\mathbf{z}|\mathbf{x}_{k|k-1}^{(n)}) w_{k|k-1}^{(n)}}$$

$$= \frac{\sum_{n=1}^{N+B} \ell(\mathbf{z}|\mathbf{x}_{k|k-1}^{(n)}) w'^{(n)}_{k|k-1} \delta_{\mathbf{x}_{k|k-1}^{(n)}}(\mathbf{x})}{\sum_{n=1}^{N+B} \ell(\mathbf{z}|\mathbf{x}_{k|k-1}^{(n)}) w'^{(n)}_{k|k-1}}$$

$$= \sum_{n=1}^{N+B} w_k^{(n)} \delta_{\mathbf{x}_{k|k-1}^{(n)}}(\mathbf{x}) \tag{42}$$

where the updated weight $w_k^{(n)}$ is

$$w_k^{(n)} = \frac{\ell(\mathbf{z}|\mathbf{x}_{k|k-1}^{(n)}) w'^{(n)}_{k|k-1}}{\sum_{n=1}^{N+B} \ell(\mathbf{z}|\mathbf{x}_{k|k-1}^{(n)}) w'^{(n)}_{k|k-1}} \tag{43}$$

The implementation of the particle filter is summarized using the pseudo-code in Algorithm 1, where lines 2–7 are the prediction steps; lines 8–12 are the correction steps; lines 13–16 are the resampling steps, in which N particles are resampled from the $N+B$ particles.

Algorithm 1 Particle filter implementation of the Bernoulli TBD filter

1: Inputs: $p_{k-1|k-1}, \{\mathbf{x}_{k-1}^{(n)}\}_{n=1}^N, \mathbf{z}$
2: $p_{k-1|k-1} \leftarrow \min\{p_{k-1|k-1}, U_p\}$
3: $p_{k|k-1} = p_b(1 - p_{k-1|k-1}) + p_s p_{k-1|k-1}$
4: Draw $\mathbf{x}_{k|k-1}^{(n)} \sim f_{k|k-1}(\mathbf{x}|\mathbf{x}_{k-1}^{(n)})$ for $n = 1, \ldots, N$
5: Draw $\mathbf{x}_{k|k-1}^{(n)} \sim b_{k|k-1}(\mathbf{x})$ for $n = N+1, \ldots, N+B$
6: $w'^{(n)}_{k|k-1} = p_s p_{k-1|k-1}/N$ for $n = 1, \ldots, N$
7: $w'^{(n)}_{k|k-1} = p_b(1-p_{k-1|k-1})/B$ for $n = N+1, \ldots, N+B$
8: Compute $\ell(\mathbf{z}|\mathbf{x}_{k|k-1}^{(n)})$ for $n = 1, \ldots, N+B$ using (30)
9: $\tilde{w}_k^{(n)} = \ell(\mathbf{z}|\mathbf{x}_{k|k-1}^{(n)}) w'^{(n)}_{k|k-1}$ for $n = 1, \ldots, N+B$
10: Compute the sum of the weights: $t = \sum_{n=1}^{N_s+N_b} \tilde{w}_k^{(n)}$
11: $p_{k|k} = t/(1 - p_{k|k-1} + t)$
12: Normalize weights: $w_k^{(n)} = \tilde{w}_k^{(n)}/t$, for $n = 1, \ldots, N+B$
13: **for** $n = 1 : N$ **do**
14: Select $j^n \in \{1, \ldots, N+B\}$ with probability $w_k^{(n)}$
15: $\mathbf{x}_k^{(n)} = \mathbf{x}_{k|k-1}^{(j^n)}$
16: **end for**
17: Return: $p_{k|k}, \{\mathbf{x}_k^{(n)}\}_{n=1}^N$

Estimator:

Target detection can be performed using $p_{k|k}$ as the test statistic. If $p_{k|k}$ exceeds the predefined threshold $\zeta \in (0, 1)$, target

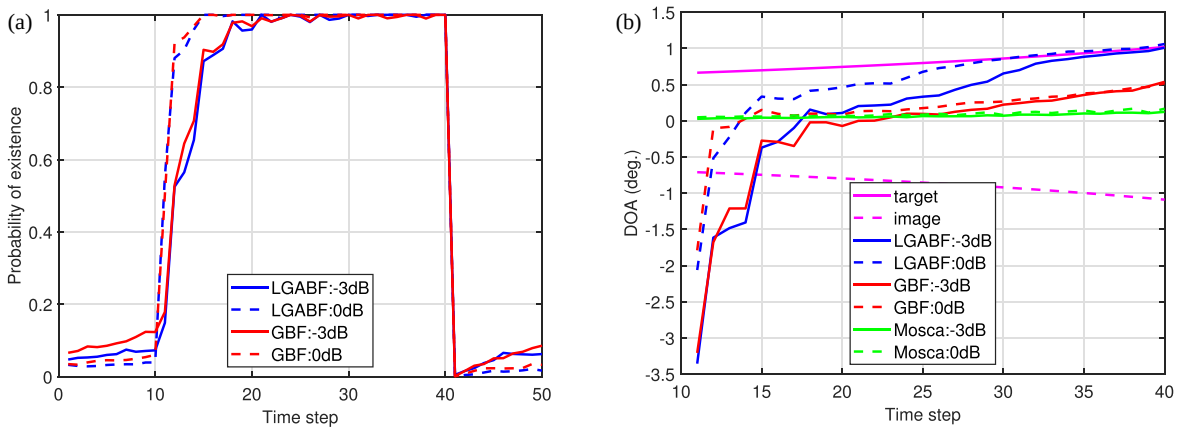

FIGURE 4. Averaged results. (a) Probability of existence. (b) DOA estimation.

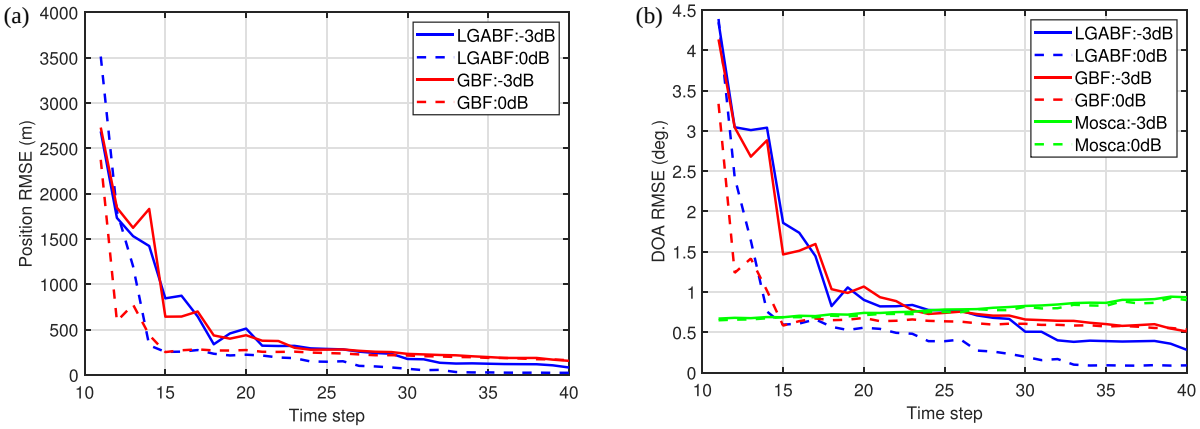

FIGURE 5. Estimation RMSEs. (a) Range RMSE. (b) DOA RMSE.

presence is declared. If a target is detected, the target state is estimated using the particles before resampling by the minimum mean-square error (MMSE) estimator:

$$\hat{\mathbf{x}}_{k|k} = \sum_{n=1}^{N+B} w_k^{(n)} \mathbf{x}_{k|k-1}^{(n)} \tag{44}$$

5. SIMULATION

In this section, performance of the proposed Bernoulli TBD filter for LGA scenario is evaluated through simulations. The proposed filter is referred to as LGABF in this section. For comparison, the general Bernoulli filter for monopulse that does not model the multipath in [36] is simulated, which is referred to as GBF.

Throughout the simulation, we set $\sigma_s^2 = \sigma_d^2 = 1$. The SNR for each pulse is defined as

$$\text{SNR} = \frac{E(\alpha_{id}^2)}{2\sigma_s^2} = \frac{E(\alpha_{id}^2)}{2\sigma_d^2} = \frac{\bar{\sigma}\kappa^2}{2r^4} \tag{45}$$

in which it is assumed that $h_{l_i}(r) = 1$ and $G_\Sigma^2(\theta) = 1$. For simplicity, we set value of the radar constant as $\kappa = r_{d0}^2$, where r_{d0} is the initial range of the target. Then, the SNR is controlled by target ARCS $\bar{\sigma}$ and target range, and the initial SNR of the target is equal to the value of $\bar{\sigma}/2$ (in m^2). The number of pulses in each dwell is $M = 40$. The specular reflection coefficient $\rho = 0.8$. The size of a slot is $\Delta R = 45$ m. The dwell interval $T = 1$ s. The radar is stationary with height $h_r = 10$ m. The target is initially located at (25, 0.3) km and flies at a constant velocity of 300 m/s toward the radar. A total of 50 time steps are used, with target introduced at time step 11 and deleted at time step 41. The particle filter parameters are as follows, birth probability $p_b = 0.05$, survival probability $p_s = 0.95$, particle number $B = 1000$ and $N = 5000$.

With 100 Monte Carlo runs, the estimation results of the two filters at different SNRs are shown in Figs. 4 and 5. The widely used monopulse DOA estimation method proposed by Mosca [41] is also used for comparing the DOA estimation performance. In Mosca method, locations of the two sampling points affected by the target are assumed to be known, and the monopulse estimation results of the two sampling points are averaged. Fig. 4(a) displays the averaged probability of existence. We observe that the target can be detected several time steps after its appearance, and the detection delay is longer for lower SNRs. The detection performances of the two filters are essentially the same. Fig. 4(b) presents the DOA estimation results. For LGABF (proposed filter), the estimated DOA converges to the true values as the time step increases, and the convergence speed is faster for higher SNRs. For GBF, however, due to its lack of multipath modeling, the DOA estimation fails.

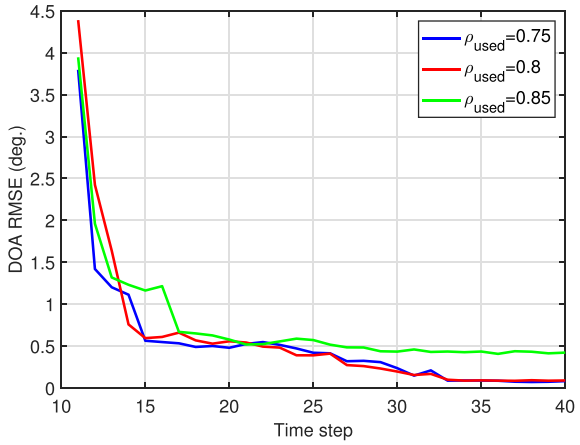

FIGURE 6. DOA RMSE of the LGABF using biased ρ, with the truth of $\rho = 0.8$, and SNR $= 0$ dB.

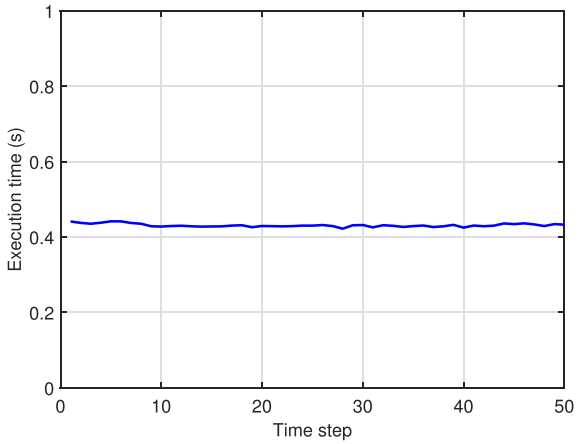

FIGURE 7. Average execution time of LGABF method.

For Mosca's method, the averaged DOA estimation result is a power weighted average of the DOAs of the target and its image. This is the reason that monopulse processing fails in a low-grazing angle scenario.

The range root mean square error (RMSE) and DOA RMSE are shown in Fig. 5(a) and Fig. 5(b), respectively. The RMSEs of the proposed filter decrease as time steps increase, and the higher the SNR is, the better the performance is. RMSEs of the GBF decrease as time steps increase too, but the decrease stops at a relatively high value because a bias exists in the estimate. In Fig. 5(b), Mosca method failed due to the multipath effect, while LGABF method converges to the ground truth as the time step increases. As time steps increase, the RMSEs of Mosca method increase because the distance between the target and power weighted centroid of the target and its image increases as shown in Fig. 4(b).

The detection performance of the proposed LGABF method is evaluated using standard detection metrics. For comparison, GBF method and the widely used non-coherent integrator [42] are evaluated simultaneously. For LGABF and GBF methods, the probability of false alarm p_F is estimated using dwells 1 to 10 where no target is present. More explicitly,

$$p_F = \frac{1}{10K_T} \sum_{i=1}^{K_T} \sum_{k=1}^{10} p_{k|k}^{i} \underset{0}{\overset{1}{\gtrless}} \zeta \tag{46}$$

where i is the index of each Monte Carlo run, and K_T is the number of Monte Carlo runs. Similarly, the probability of detection p_D is computed as

$$p_D = \frac{1}{20K_T} \sum_{i=1}^{K_T} \sum_{k=21}^{40} p_{k|k}^{i} \underset{0}{\overset{1}{\gtrless}} \zeta \tag{47}$$

Since both the LGABF and GBF methods declare a detection per dwell, to ensure fairness, the non-coherent integrator's detection criterion is defined as at least one sampling point exceeding the threshold after non-coherent integration. Thus, the corresponding probability of false alarm for each sampling point is given by $1 - (1 - p_F)^L$. Table 1 compares the detection performance of all three methods across varying SNRs.

TABLE 1. Detection performance.

SNR	p_F	p_D (-3 dB)	p_D (0 dB)
Non-coherent integrator	0.003	0.5939	0.9019
GBF	0.003	0.9940	0.9995
LGABF	0.001	0.9955	0.9995

For LGABF and GBF methods, the threshold is set to $\zeta = 0.6$. The non-coherent integrator's threshold is calibrated to match the GBF method's p_F. As shown in Table 1, LGABF method demonstrates a significant improvement in detection performance compared to the non-coherent integrator and a marginal enhancement over the GBF method.

LGABF and GBF methods are both designed for dim target detection and tracking. Simulation results demonstrate that both methods enhance detection performance compared to non-coherent integration approach. However, LGABF explicitly models multipath effects, whereas GBF does not. Thus, the primary advantage of LGABF over GBF lies in its DOA estimation accuracy under low-grazing angle conditions.

To analyze the robustness of the proposed method against environmental uncertainty, Fig. 6 illustrates the DOA estimation performance of LGABF when using a biased ρ value. The true value of ρ is set to 0.8, while the filter employs three biased values: $\rho_{\text{used}} = 0.75$, 0.8, and 0.85. It is evident that the estimation performance degrades as the used ρ deviates from the true value, particularly when $\rho_{\text{used}} = 0.85$. These results demonstrate that the realistic modeling of multipath effects is critical for optimal performance.

The average execution time of the proposed filter is presented in Fig. 7. All simulations are executed on a laptop with Intel i5-12450H CPU and 16 GB RAM by MATLAB R2023a. The filter achieves an average execution time of 0.43 seconds per time step. If the proposed method is programmed in C language, it can run much faster than in MATLAB (in the order of a few tens times faster) [43]. This computational efficiency renders the proposed method suitable for real-time processing in practical scenarios.

6. CONCLUSIONS

This article proposes a Bernoulli TBD filter for low-grazing angle tracking with monopulse radar. Using multipath model and Swerling II radar target model, the measurements generated by a single target and its multipath image are modeled. The measurement model is incorporated into the Bernoulli TBD filter and implemented using particle filter. Simulation results show that the proposed filter can efficiently detect and track a dim target in low-grazing scenario. On the contrary, the Bernoulli TBD filter that does not model the multipath failed to track the target.

ACKNOWLEDGEMENT

This work was supported by the ATR Laboratory Fund under Grant WDZC20245250205.

REFERENCES

[1] Sen, S. and A. Nehorai, "OFDM MIMO radar with mutual-information waveform design for low-grazing angle tracking," *IEEE Transactions on Signal Processing*, Vol. 58, No. 6, 3152–3162, 2010.

[2] Zhang, H., J. Yan, W. Liu, and Q. Zhang, "Array scheduling with power and bandwidth allocation for simultaneous multibeam tracking low-angle targets in a VHF-MIMO radar," *IEEE Transactions on Aerospace and Electronic Systems*, Vol. 59, No. 5, 5714–5730, 2023.

[3] Sebt, M. A., M. Goodarzi, and H. Darvishi, "Geometric arithmetic mean method for low altitude target elevation angle tracking," *IEEE Transactions on Aerospace and Electronic Systems*, Vol. 59, No. 5, 5111–5119, 2023.

[4] Blair, W. D. and M. Brandt-Pearce, "Unresolved Rayleigh target detection using monopulse measurements," *IEEE Transactions on Aerospace and Electronic Systems*, Vol. 34, No. 2, 543–552, 1998.

[5] Glass, J. D. and W. D. Blair, "Detection of unresolved Rayleigh targets using adjacent bins," in *2016 IEEE Aerospace Conference*, 1–7, Big Sky, MT, USA, Mar. 2016.

[6] Cai, F., "Unresolved Rayleigh targets detection for monopulse radar with knowledge of one target's DOA," *IEEE Transactions on Aerospace and Electronic Systems*, Vol. 60, No. 6, 9411–9417, Dec. 2024.

[7] Cai, F. and H. Fan, "Detection of unresolved Rayleigh targets in monopulse radar with two angular dimensions," *IEEE Transactions on Aerospace and Electronic Systems*, 2025.

[8] Blair, W. D. and M. Brandt-Pearce, "Monopulse DOA estimation of two unresolved Rayleigh targets," *IEEE Transactions on Aerospace and Electronic Systems*, Vol. 37, No. 2, 452–469, Apr. 2001.

[9] Wang, Z., A. Sinha, P. Willett, and Y. Bar-Shalom, "Angle estimation for two unresolved targets with monopulse radar," *IEEE Transactions on Aerospace and Electronic Systems*, Vol. 40, No. 3, 998–1019, 2004.

[10] Zhang, X., P. K. Willett, and Y. Bar-Shalom, "Monopulse radar detection and localization of multiple unresolved targets via joint bin processing," *IEEE Transactions on Signal Processing*, Vol. 53, No. 4, 1225–1236, Apr. 2005.

[11] Lee, S.-P., B.-L. Cho, S.-M. Lee, J.-E. Kim, and Y.-S. Kim, "Unambiguous angle estimation of unresolved targets in monopulse radar," *IEEE Transactions on Aerospace and Electronic Systems*, Vol. 51, No. 2, 1170–1177, Apr. 2015.

[12] Wang, S. L., Z.-H. Xu, X. Yang, Z. Li, and G. Wang, "Efficient and unambiguous two-target resolution via subarray-based four-channel monopulse," *IEEE Transactions on Signal Processing*, Vol. 68, 885–900, 2020.

[13] Nandakumaran, N., A. Sinha, and T. Kirubarajan, "Joint detection and tracking of unresolved targets with monopulse radar," *IEEE Transactions on Aerospace and Electronic Systems*, Vol. 44, No. 4, 1326–1341, 2008.

[14] Isaac, A., P. Willett, and Y. Bar-Shalom, "Quickest detection and tracking of spawning targets using monopulse radar channel signals," *IEEE Transactions on Signal Processing*, Vol. 56, No. 3, 1302–1308, 2008.

[15] Huang, Q., H. Fan, F. Cai, and H. Xiao, "Joint estimation of unresolved leader-follower in the presence of dense false signals using monopulse radar," *IEEE Transactions on Aerospace and Electronic Systems*, Vol. 59, No. 6, 9635–9649, 2023.

[16] Zoltowski, M. D. and T.-S. Lee, "Maximum likelihood based sensor array signal processing in the beamspace domain for low angle radar tracking," *IEEE Transactions on Signal Processing*, Vol. 39, No. 3, 656–671, 1991.

[17] Djeddou, M., A. Belouchrani, and S. Aouada, "Maximum likelihood angle-frequency estimation in partially known correlated noise for low-elevation targets," *IEEE Transactions on Signal Processing*, Vol. 53, No. 8, 3057–3064, Aug. 2005.

[18] Sherman, S. M., "Complex indicated angles applied to unresolved radar targets and multipath," *IEEE Transactions on Aerospace and Electronic Systems*, Vol. 7, No. 1, 160–170, 1971.

[19] Xu, Z., Z. Xiong, J. Wu, and S. Xiao, "Symmetrical difference pattern monopulse for low-angle tracking with array radar," *IEEE Transactions on Aerospace and Electronic Systems*, Vol. 52, No. 6, 2676–2684, 2016.

[20] Shi, X., A. Taheri, T. Çeçen, and N. Çelik, "Particle filtering-based low-elevation target tracking with multipath interference over the ocean surface," *IEEE Transactions on Aerospace and Electronic Systems*, Vol. 56, No. 4, 3044–3054, 2020.

[21] Wu, P., J. Chen, S. Guo, G. Cui, L. Kong, and X. Yang, "NLOS positioning for building layout and target based on association and hypothesis method," *IEEE Transactions on Geoscience and Remote Sensing*, Vol. 61, 1–13, 2023.

[22] Pham, B.-H., O. Rabaste, J. Bosse, I. Hinostroza, and T. Chonavel, ""Around-the-Corner" radar: Particle filters for non-line-of-sight target tracking in the presence of ambiguities," *IEEE Transactions on Aerospace and Electronic Systems*, 1–15, 2024.

[23] Barniv, Y., "Dynamic programming solution for detecting dim moving targets," *IEEE Transactions on Aerospace and Electronic Systems*, Vol. 21, No. 1, 144–156, 1985.

[24] Carlson, B. D., E. D. Evans, and S. L. Wilson, "Search radar detection and track with the Hough transform. I. System concept," *IEEE Transactions on Aerospace and Electronic Systems*, Vol. 30, No. 1, 102–108, 1994.

[25] Rutten, M. G., B. Ristic, and N. J. Gordon, "A comparison of particle filters for recursive track-before-detect," in *2005 7th International Conference on Information Fusion*, Vol. 1, 7–pp, Philadelphia, PA, USA, Jul. 2005.

[26] Salmond, D. J. and H. Birch, "A particle filter for track-before-detect," in *Proceedings of the 2001 American Control Conference (Cat. No.01CH37148)*, Vol. 5, 3755–3760, Arlington, VA, USA, 2001.

[27] Rutten, M. G., N. J. Gordon, and S. Maskell, "Recursive track-before-detect with target amplitude fluctuations," *IEE Proceedings — Radar, Sonar and Navigation*, Vol. 152, No. 5, 345–352,

Oct. 2005.

[28] Zheng, S., D. Li, Q. Yang, Y. Zhao, L. Jiang, and Z. Wang, "A log-normal complex-amplitude likelihood ratio-based TBD method with soft orbit-information constraints for tracking space targets with space-based radar," *IEEE Transactions on Radar Systems*, Vol. 3, 467–482, 2025.

[29] Streit, R. L., M. L. Graham, and M. J. Walsh, "Multitarget tracking of distributed targets using histogram-PMHT," *Digital Signal Processing*, Vol. 12, No. 2-3, 394–404, 2002.

[30] Mahler, R., *Statistical Multisource-Multitarget Information Fusion*, Artech House, Boston, 2007.

[31] Ristic, B., B.-T. Vo, B.-N. Vo, and A. Farina, "A tutorial on Bernoulli filters: Theory, implementation and applications," *IEEE Transactions on Signal Processing*, Vol. 61, No. 13, 3406–3430, Jul. 2013.

[32] Wong, S., B. T. Vo, and F. Papi, "Bernoulli forward-backward smoothing for track-before-detect," *IEEE Signal Processing Letters*, Vol. 21, No. 6, 727–731, 2014.

[33] Papi, F., V. Kyovtorov, R. Giuliani, F. Oliveri, and D. Tarchi, "Bernoulli filter for track-before-detect using MIMO radar," *IEEE Signal Processing Letters*, Vol. 21, No. 9, 1145–1149, Sep. 2014.

[34] Kim, D. Y., B. Ristic, R. Guan, and L. Rosenberg, "A Bernoulli track-before-detect filter for interacting targets in maritime radar," *IEEE Transactions on Aerospace and Electronic Systems*, Vol. 57, No. 3, 1981–1991, 2021.

[35] Ristic, B., D. Y. Kim, L. Rosenberg, and R. Guan, "Exploiting Doppler in Bernoulli track-before-detect for a scanning maritime radar," *IEEE Transactions on Aerospace and Electronic Systems*, Vol. 58, No. 1, 720–728, 2022.

[36] Cai, F., "Monopulse radar track-before-detect using Bernoulli filter," *IET Signal Processing*, Vol. 16, No. 8, 1011–1021, Jul. 2022.

[37] Üney, M., P. Horridge, B. Mulgrew, and S. Maskell, "Coherent long-time integration and Bayesian detection with Bernoulli track-before-detect," *IEEE Signal Processing Letters*, Vol. 30, 239–243, 2023.

[38] Li, X. R. and V. P. Jilkov, "Survey of maneuvering target tracking. Part I. Dynamic models," *IEEE Transactions on Aerospace and Electronic Systems*, Vol. 39, No. 4, 1333–1364, 2003.

[39] Richards, M. A., *Fundamentals of Radar Signal Processing*, 2nd ed., McGraw-Hill, New York, NY, USA, 2014.

[40] Skolnik, M. I., *Introduction to Radar Systems*, 3rd ed., McGraw-Hill, New York, 2001.

[41] Mosca, E., "Angle estimation in amplitude comparison monopulse systems," *IEEE Transactions on Aerospace and Electronic Systems*, No. 2, 205–212, Mar. 1969.

[42] Skolnik, M. I., *Radar Handbook*, 3rd ed., McGraw-Hill, New York, 2008.

[43] Zhang, X., P. Willett, and Y. Bar-Shalom, "Detection and localization of multiple unresolved extended targets via monopulse radar signal processing," *IEEE Transactions on Aerospace and Electronic Systems*, Vol. 45, No. 2, 455–472, Apr. 2009.